Ahmed, J., Peakall, J., Balme, M.R., and Parsons, D.R., 2023, Rapid megaflood-triggered base-level rise on Mars: Geology, https://doi.org/10.1130/ G50277.1

Supplemental Materials

Topographic analysis

The inferred position of a multi-age composite channel centerline and clearly visible cutoff meanders for a 22.6 km stacked channel sequence (AD1) in the Aeolis Dorsa were digitized from the HiRISE DEM (**Fig. 1B**). The DEM was created using HiRISE stereo image pair PSP_006683_1740 and PSP_010322_1740 following the SOCET SET commercial processing pipeline (Kirk et al., 2008). The channel sequence is comprised of at least two distinct channels separated by an abrupt transition to steeper lateral accretion package (LAP) deposits downstream of meander 8 (**background color change**, **Fig. 1B & Fig. 1C**). These channel segments also separate point-bar sequences whose lowermost parts start at heights that are 40-60 meters apart (**Fig. S1**), representing two stacked channels.

The identification of multiple stacked channels and the position of the change in channel age is consistent with the avulsion point and stratigraphic evidence presented by Cardenas et al. (2018). Cardenas et al. (2018) employed a method to quantify meander asymmetry developed by Carson and Lapointe (1983) to resolve the flow direction of the meanders on AD1. Their results showed that the channel flow direction was from north to south, despite the modern surface topography suggesting a northward flow. This apparent contradiction is considered the result of differential erosion, which has exposed older deposits to the north and not from post-depositional tectonics (DiBiase et al., 2013; Cardenas et al., 2018). There may also have been influence from the loading induced by Tharsis (Bouley et al., 2016), however this long-wavelength deformation, if present, will affect all of the deposits, and will therefore not affect intra-slope variations. This can be demonstrated using the map of Tharsis-induced elevation change reported by Citron et al. (2018; their extended data figure 2). Aeolis Dorsa is positioned on the contour of 0 km elevation change; however, ±1 km elevation changes are expected 1200 km to the east and west of Aeolis Dorsa. This suggests that a negligible slope variation of 0.0008 could affect the deposits (1 km over 1200 km). Where the impact of long-wavelength deformations may be more important is in estimates of basin filling and system-wide subsidence due to tectonic tilting or compaction (Lefort et al., 2012; Citron et al., 2018).

Sinuosity was computed using the ratio of channel length to segmented-valley length, while channel widths were determined by measuring the straight-line distance orthogonal to the preserved channel caprock at straight sections of the channel ($n_{measurements}$ = 39). We acknowledge that the use of the caprock to estimate channel dimensions may yield inaccuracies due to poor preservation of the original channel or preservation of multiple channels within the caprock (Hayden et al., 2019; Hayden and Lamb, 2020). However, in this case the consistent orientation of LASs with the channel caprock, and the completeness of the LASs, indicates that this is a channel-form rather than a channel-belt.

Average profiles were derived by computing the mean change in elevation at *ca*. 1 m intervals along the transects (**Fig. 2A&B).** This generated artefacts with distance along the transects as the number of profiles being averaged-over diminished, resulting in abrupt changes in elevation. These artefacts only presented a challenge for data visualization as the full dataset was used in subsequent phases of analysis. Profiles across point-bar deposits may be affected by differential erosion, and in turn this may reflect primary variations in facies across point-bars. However, the analysed bends are dominated by bend

expansion, with very limited bend rotation. Numerical simulations of such bends suggest that point bars have the lowest spatial variability in sand fraction (Yan et al., 2021). Furthermore, the overall sand fraction in the numerical model for such bends was 94% (Yan et al., 2021) suggesting that, model assumptions aside, these simple expansional bend geometries are unlikely to be affected by significant variations in original point-bar facies that might be exploited by subsequent differential erosion.

Calculating between-LAS elevation changes

Lateral accretion surfaces were identified using the adaptive thresholding strategy after finding good correspondence between the manual and automated identification of lateral accretion surfaces and packages from the HiRISE DEM (**see Figs S3&S4**). The thresholded image was superimposed over the HiRISE DEM in a geographic information system (ArcGIS 10.4) and used to identify lateral accretion surfaces. The thresholded image made bar identification from the DEM easier by enhancing areas that were otherwise unclear. Once the lateral accretion surfaces had been digitized, equidistant points were created along each bar at 1 m intervals and used to extract the surface elevation from the underlying HiRISE DEM described above (**Fig. S4**). The elevation distributions from each lateral accretion surface on each meander were compiled and descriptive statistics were computed (median, interquartile range, and 10th and 90th percentiles). The elevation reflecting the 90th percentile for each lateral accretion surface was used to compute the elevation change between the subsequent lateral accretion packages (i.e., $Z_{n+1} - Z_{n,}$ where Z is the elevation). The 90th percentile was chosen as it is assumed to represent the maximum elevation of the lateral accretion surfaces, thus providing a closer estimate of bar elevation prior to deflation. Equally, these measurements are likely conservative estimates of aggradation, since sediment compaction cannot be accounted for without a deeper knowledge of the stratigraphy and further field reconnaissance.

Derivations of Martian channel depth and grain size measurements

We used a numerical framework proposed by Lapôtre et al. (2019) that developed the work of Konsoer et al. (2018) to estimate bankfull discharge, channel depth, slope, and grain size from direct measurements of width from AD1. Below we specify the calculations and values derived.

From Konsoer et al. (2018) (their Fig. 2),

$$Q = 0.2B^{1.68} \quad (1)$$

$$H = 0.164B^{0.66} \quad (2)$$

Where Q is bankfull discharge (m^3 s^{-1}), B is average channel width (38.8 m), and H is channel depth in meters. Using the derived values of Q, B, and H, we subsequently calculated the width to depth ratio (B:H) and channel slope (s) from Lapôtre et al. (2019) (their equation 15) using the following,

$$s \approx 9.1 \frac{C_f}{g_M} B^{-0.62} \quad (3)$$

where C_f is assumed to approximate 0.002 after Wright and Parker (2004) and g_M is

gravitational acceleration on Mars (3.72 m^2 s^{-1}).

Given the reduced gravity on Mars (0.38g_{Earth}), steeper channel bed slopes are required to develop sufficient shear stresses at the banks and to erode and produce planform geometry like those observed on Earth. The degree of slope increase required to erode Martian riverbanks is also contingent on the caliber of bank materials. As such, finer and coarser grains require higher shear stresses to be eroded than do intermediate unconsolidated grains. We used a stability field diagram (**Fig. S6**) adapted from Lapôtre et al. (2019) and our estimate of channel slope (*s*) and channel aspect ratio (*B:H*, 21.2) for AD1 to establish the grain size for the channel (**black star, Fig S6**). The presence of fine-grained clays and silts are consistent with theories of bank stabilization in the absence of vegetation (Peakall et al., 2007; Matsubara et al., 2015; Santos et al., 2019; Li et al., 2019; Ielpi et al., 2022) and with the preferential removal of these sediments by aeolian erosion, which was responsible for exhuming the coarse-grained channel deposits (Burr et al., 2010).

Backwater length effects

At the transition between terrestrial river systems and their receiving basins the channel flow depth increases, which causes a reduction in flow velocity; the distance over which this deepening occurs is the backwater length (Chow, 1959). This reduction in flow velocity alters sediment transport and channel morphology over the length of the backwater zone extending from the receiving basin (Nittrouer et al., 2012). Lateral channel mobility typically decreases in favor of vertical aggradation in this zone (Blum et al., 2013). The backwater length can be estimated by dividing channel depth (*H*) by channel slope (*s*) (Bresse, 1860; Lamb et al., 2012). Employing our estimates of depth and slope for AD1 (**Table S4**), we estimated the length of the backwater zone to be ~ 3.66 km using our average caprock width (**Table S5**). However, we also tested the backwater length calculation with our measured width values at the 10^{th} and 90^{th} percentiles (**Table S5**) to establish the range of possible backwater lengths for AD1 (1.69 - 6.56 km). Additionally, after Hayden and Lamb (2020) posited that up to 90% of the preserved caprock width may have been eroded, we computed the necessary caprock widths required to satisfy the measured ~40 km backwater length upstream of the delta deposits described by Hughes et al. (2019) (**Fig. S6**). We projected 0-90% width increases on our measured 10^{th}, 50^{th}, and 90^{th} percentile width measurements and determined that all three required >70% channel width increases to generate backwater length of ~40 km (**Fig. S6**). Therefore, the data suggest that the deposits on AD1 were likely not influenced by backwater hydrodynamics. This is also supported by significant lateral channel mobility on the reach (**Table S5**), which is typically observed to be suppressed in the backwater zone (Blum et al., 2013), although exceptions to this relationship have been observed (Swartz et al., 2020).

Derivation of continuous bankfull (non-episodic) meander migration rate

Ielpi and Lapôtre (2020) derived an approximation for channel migration using a global compilation of measurements from across a range of climates. The results revealed that, when averaged over multiple years, channel migration rates could be scaled by channel width using a power law. Two distinct power law relationships were derived for vegetated and unvegetated systems and demonstrated that rivers in barren landscapes migrated by an order of magnitude more quickly than rivers in vegetated landscapes (Ielpi and Lapôtre,

2020). Since channel migration in barren landscapes is principally controlled by excess shear stress at the channel bank, and that this is driven by discharge, channel width (*B*) was found to provide a reliable approximation for this. As such, Lapôtre and Ielpi (2020) derived the following relationship for the migration rate of non-vegetated rivers ($M_{R,nv}$):

$$M_{R,nv} \approx (0.133 \pm 0.006)B^{0.85} \quad (4)$$

Developing this relationship further for application to Martian rivers, Lapôtre and Ielpi (2020) developed an equation for the bankfull channel migration rate ($M_{R,\ nv\text{-}BF}$) that accounted for the assumption that most geomorphic work – in this case bank erosion – is accomplished during bankfull discharge and that between these intermittent phases of activity, little geomorphic work is completed. Finally, to account for the reduced gravitational forces on Mars, the bank erosion equation was scaled to,

$$M_{R,M,BF} \approx 9.81B^{0.85} \quad (5)$$

where, $M_{R,M,BF}$ is the bankfull (or continuous bankfull, non-episodic) Martian meander migration rate in units of meters per Earth year (m yr^{-1}).

We used the derivation in equation 5 to estimate the bankfull Martian meander migration rate to estimate rates of channel migration for channel AD1 using the average channel width measured from the inferred most recent preserved channel. We also estimated the range in migration rates by substituting the average channel width at the 10^{th} and 90^{th} percentiles (**Table S5**) as computed from the 38 discrete measurements of channel width.

Aggradational inner-bend topography or erosionally induced inner bend topography?

The thicknesses of the LAPs can be combined with the channel width measurements and depth estimates, as described earlier, in order to examine this question as to what the inner-bend topography represents. As argued earlier, these lateral accretion packages are from individual meanders that have dominantly undergone bend expansion. If the observed inner-bend topography was purely the product of erosion then that would imply that the lateral accretion packages were originally up to 14.4 meters thick (average 5.7 meters) and that they have since been eroded to give these profiles. Given that channel width is on average 38.8 meters and that the estimated channel depth is 1.83 meters, based on the equation in Konsoer et al. (2018) (see above), then that indicates that such thick lateral accretion packages are not tenable. Any errors in channel width measurement as a result of possible erosion, are likely far too small to produce channel depths that could generate lateral accretion packages comparable to these thicknesses. Instead, these relationships imply that these inner bend deposits were strongly aggradational – multiples of channel depth.

The stepped nature of the stratigraphy that coincides with individual lateral accretion packages does imply that there was a marked contrast in deposit type that has been acted upon by erosional processes. Such contrasts are prominent at the top of lateral accretion packages where they are overlain by finer-grained and more erodible scroll bar ridge-and-swale topography (e.g., Shiers et al., 2019; Hayden and Lamb, 2020). However, if this were instead a section through the lateral accretion packages generated by a meander undergoing simple bend expansion then such internal sedimentary contrasts would not be

expected (e.g., Willis and Tang, 2010). We therefore conclude that there is good evidence for the exceptional aggradational nature of these channels, and that the observed morphology and topography represent exhumed lateral accretion packages.

Superelevation index

We quantify this aggradation using a superelevation index (S_E). This is calculated by taking the height from the lowest point of the inner-bend deposits to the caprock crest, h_i. However, this height value only measures from the deposit surface representing the uppermost parts of the LAP. Therefore, the thickness of the LAP at the basal point, ~H (Leeder, 1973), needs to be accounted for, to give a total height of h_i+H. This can then be divided by the estimated channel depth H, to give (h_i+H)/H (**Fig.S5**). This can be compared to values of the superelevation index calculated for an existing database of subaerial and submarine channels (Jobe et al., 2020; **Fig.3B; Tables S2&S3**), based on their levee thickness divided by channel depth (**Fig.S5**). The definition used herein for the Aeolis Dorsa channels is comparable in terms of the calculated heights to the expression used by Jobe et al. (2020) for rivers assuming that the channel filled up to the bankfull level of the levee-crest; an S_E value of 1 representing no aggradation.

Superelevation, aggradation rate and avulsion frequency

Avulsions have been linked to both aggradation rate (e.g., Jerolmack and Mohrig, 2007; Ganti et al., 2016) and superelevation index (e.g., Mohrig et al., 2000; Hajek and Wolinsky, 2012). In the latter case, Mohrig et al. (2000) found that rivers tended to avulse when they had superelevation above the surrounding floodplain equivalent to approximately one channel depth; this corresponds to a superelevation index, S_E, of 2 as used by Jobe et al. (2020) and herein (see above). Consequently, the median and maximum S_E values of 3.95 and 7.97 calculated from the AD1 channel are highly anomalous; it would be expected that the AD1 channel should have avulsed well before reaching the present elevation. Jerolmack and Mohrig (2007) further argued that avulsion occurs where lateral channel migration is small relative to vertical aggradation above the floodplain. They defined an avulsion timescale, T_A, that was equal to H/V_A where V_A is vertical aggradation rate, and then compared this to lateral migration rates. Lapôtre and Ielpi (2020) then modified this expression for Mars and linked to channel width, B, and $M_{R,M,BF}$, the bankfull (or continuous bankfull, non-episodic) Martian meander migration rate (see earlier) to give $T_A = B/M_{R,M,BF}$. Taking channel width, B, of 38.8 m and median $M_{R,M,BF}$ of 219.9 m (**Table S5**) gives an avulsion timescale of ~5.7 years. So irrespective of avulsion criterion, superelevation, or aggradation rate versus lateral mobility, the AD1 channels are highly anomalous, and indicate very rapid aggradation that has allowed these very high superelevations in the absence of avulsion. As noted in the main text we attribute this to rapid sedimentation associated with rapid base-level change.

Sources of water for basin filling: fluvial supply or externally sourced megafloods?

The observed superelevation of AD1, and the evidence for the rapidity of this aggradation, is

argued herein to represent a rapid-rise in base-level. Yet how were these rising water-levels sourced, from the flows transiting AD1 or from an external source of water that filled the basin that AD1 flowed into?

For the case of basin filling by the same flows that formed AD1, flows would likely be supplied during warming periods through episodic rainfall events that have been purported during the Late Noachian and Early Hesperian (Kite et al., 2013; Wordsworth et al., 2017; Liu et al., 2021), or from groundwater seepage (Salese et al., 2020). For AD1 at constant bankfull flow (93.38 $m^3 s^{-1}$), the basin would fill at rate of ~5.5 km^3 Mars-yr^{-1}, with a total filling time of ~5-43 Mars-yrs, for illustrative basins a, b, and c (**see Table S7 and Fig. S8**). However, evaporation loss rates from lakes on Earth are typically meters per year, which is compatible with previous Mars modeling (Morton, 1983; Buhler et al., 2014). Taking a conservative value of 1 meter of evaporative loss per Martian year, would mean that evaporative losses would represent ~90% of water delivered from AD1 for basin a, and that evaporative losses would far exceed the input for basins b and c (**Table S8 and Fig. S8**). Consequently, AD1 is unlikely to be the source for these rapidly rising base levels. There may have been other channel systems feeding these illustrative basins, but it would have taken ~4-7 channels equivalent to AD1 all flowing at constant bankfull discharge, just to match a 1 m evaporative loss rate for basins b and c. Filling these basins rapidly, would have taken many more channels (**Fig. S8**).

Given the likely evaporative losses, AD1 could not have been the source of the rapidly rising base levels, and it would have required a network of similar sized channels all operating at constant bankfull flow levels (a highly unrealistic assumption – see the section on flow intermittency in the main text) to account for such a process. Coupled to the lack of evidence for such a channel network, suggests that this this is a very unlikely scenario. We therefore conclude that an external source of water was required to fill the basin and account for rapid base-level rise. Given the plausible sizes of basins that AD1 flowed into, it could only have been filled by extreme events, in the form of megafloods.

Basin volume and depth estimate derivations

In the following section, we describe the method for calculating basin volume and depth for our three simplified illustrative basins (a, b, c; **Fig. 1A**). The basin areas were established from the outlines in **Fig. 1A** and coupled with the average elevation rise measured from the aggradational topography on AD1 (5.72 m rounded to 6 m). The sites of these illustrative basins compares well to the most recent geological map of Aeolis Dorsa (Burr et al., 2021) and with nearby enclosed basins identified by Rivera-Hernandez and Palucis (2019). Using these measured variables, we first determined the volume of water required to fill each basin to raise the water level by 6 m. The equations and variables used in each of the equations are presented below.

Estimated megaflood volume to raise basin a (see **Fig. 4** and **Table S6**) by 6 m (average aggradational elevation change in each sequence of stacked LAPs)
Variables

a_{area} = Estimated area of basin (a, b, or c)

D_{water} = Change in depth of water caused by the flood

V_{flooda} = Flood volume for basin a, b, or c, computed as: a_{area} x D_{water}

Estimated megaflood volume to raise basin a by 6 m (average aggradational elevation change on AD1)

a_{area} = 5000 km^2

D_{water} = 0.006 km

V_{flooda} = 5000 x 0.006

V_{flooda} = 30 km^3

Estimated megaflood volume to raise basin b by 6 m (average aggradational elevation change on AD1)

b_{area} = 20,000 km^2

D_{water} = 0.006 km

V_{floodb} = 20,000 x 0.006

V_{floodb} = 120 km^3

Estimated megaflood volume to raise basin c by 6 m (average aggradational elevation change on AD1)

c_{area} = 40,000 km^2

D_{water} = 0.006 km

V_{floodc} = 40,000 x 0.006

V_{floodc} = 240 km^3

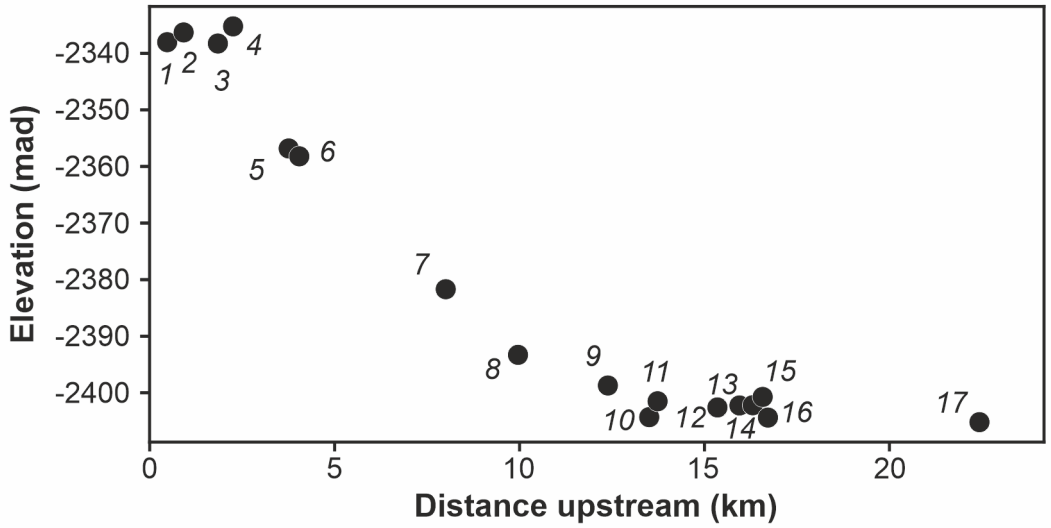

Figure S1. Initial elevations for each LAP with distance upsteam. Elevations are in meters above datum. The labeled numbers correspond to the labeled meanders in **Fig. 1B**.

Ahmed, J., Peakall, J., Balme, M.R., and Parsons, D.R., 2023, Rapid megaflood-triggered base-level rise on Mars: Geology, https://doi.org/10.1130/ G50277.1

Fig. S2. Individual elevation profiles taken across two Martian meanders. Each colored line represents a cross-LAP elevation profile. Profiles emanate in the center of the meander and terminate on the crest of the caprock.

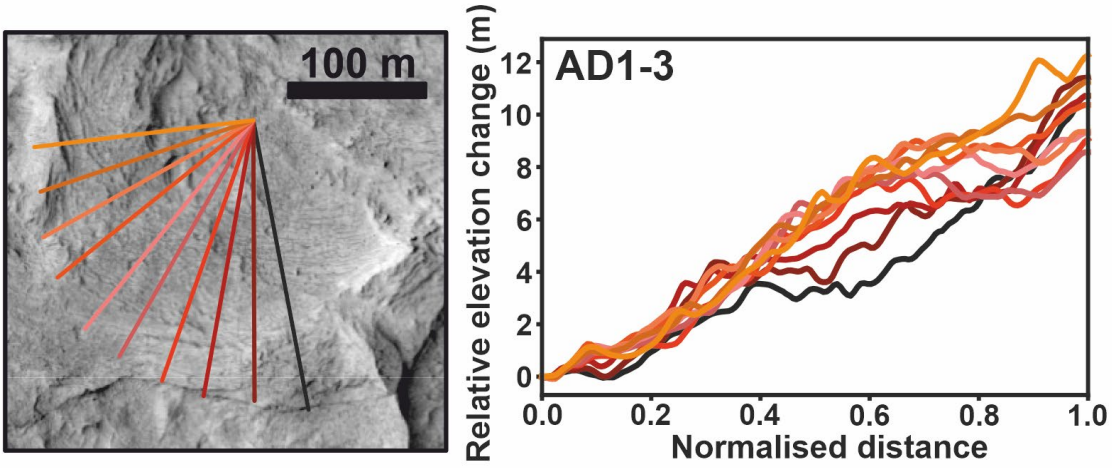

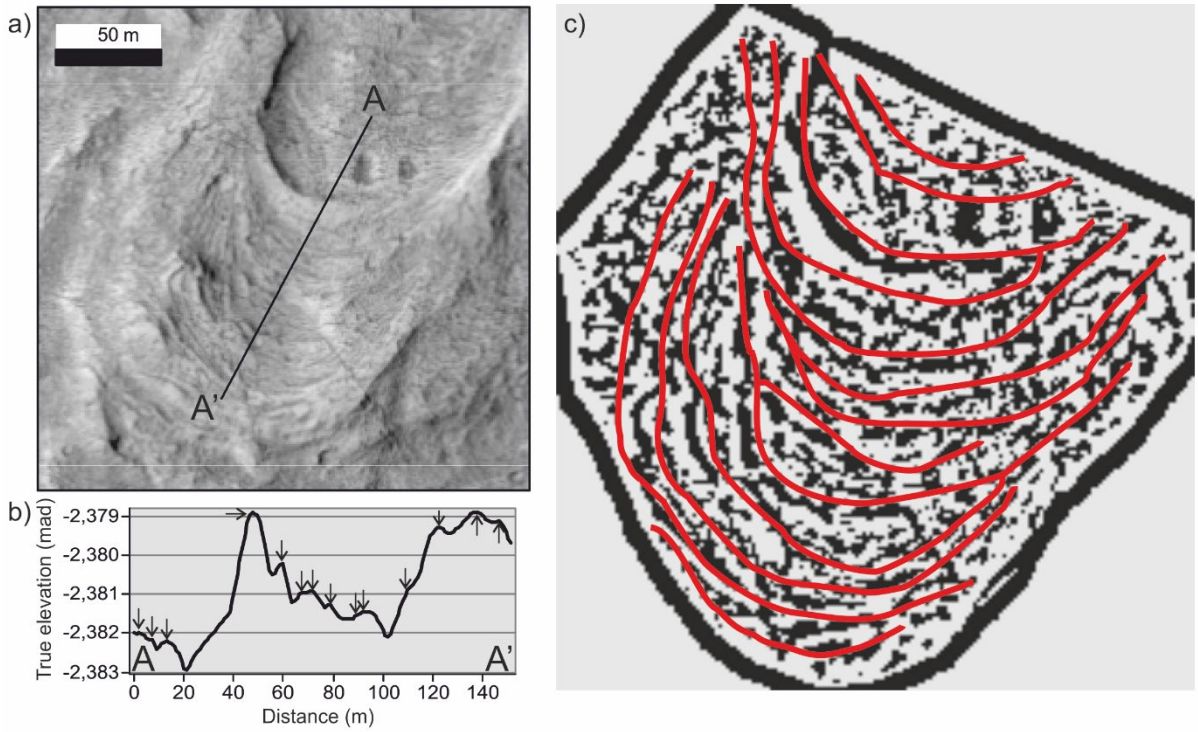

Figure S3. Methods of lateral accretion surface detection. a) 1 m resolution grayscale HiRISE digital elevation model focused on meander AD1-7 (see **Fig. 1B** for reach location). The black line indicates the cross-sectional profile taken across the lateral accretion packages. b) Cross-sectional elevation profile corresponding to the transect displayed in panel a. Elevation values are in meters above datum (mad) and black arrows indicate the location of LASs as identified by peaks in the profile. The large excursion at ca. 50 m may represent another channel location. c) LASs identified using adaptive thresholding (OpenCV, 2021). Black and white areas in the binary image recognize higher and lower parts of LAPs respectively. Red lines were added subsequently to manually delineate LASs. The total number of LASs is likely to be an underestimate due to difficulty in identifying continuous surfaces from the eroded topography.

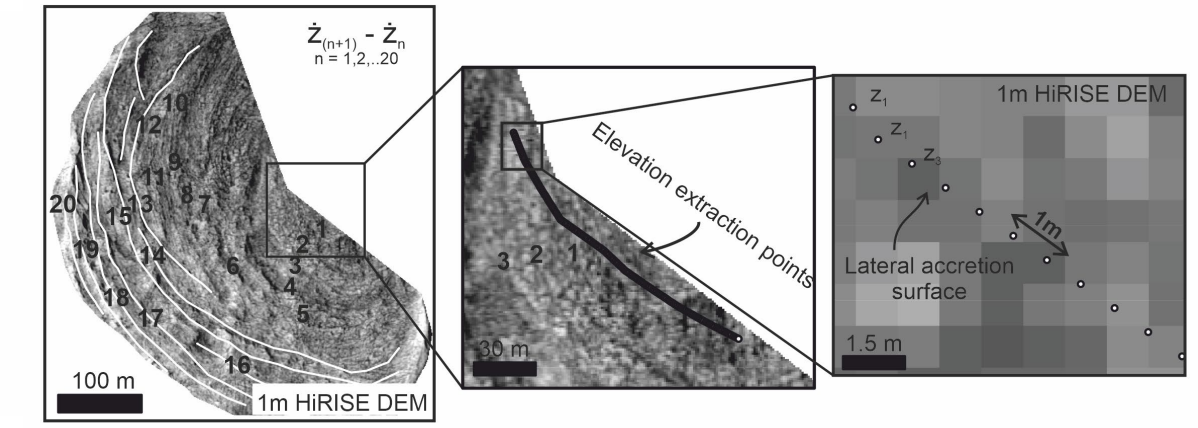

Figure S4. Methods for detecting elevation changes between LASs. Digitized LASs (white lineations) are labeled in sequence from the inside to outside of meander AD1-8. Equation denotes the calculation to deduce elevation changes between sequential surfaces where *z* is the elevation at the 90th percentile and *n* is the number of the LAS in the sequence. *ż* is the average elevation along each LAS. Outset central panel highlights the equidistant points for the first LAS on AD1-8 and is shown at higher resolution in the far-right panel where points are spaced at 1 m intervals along the digitized LAS. Each panel is overlain on the 1 m HiRISE DEM described above.

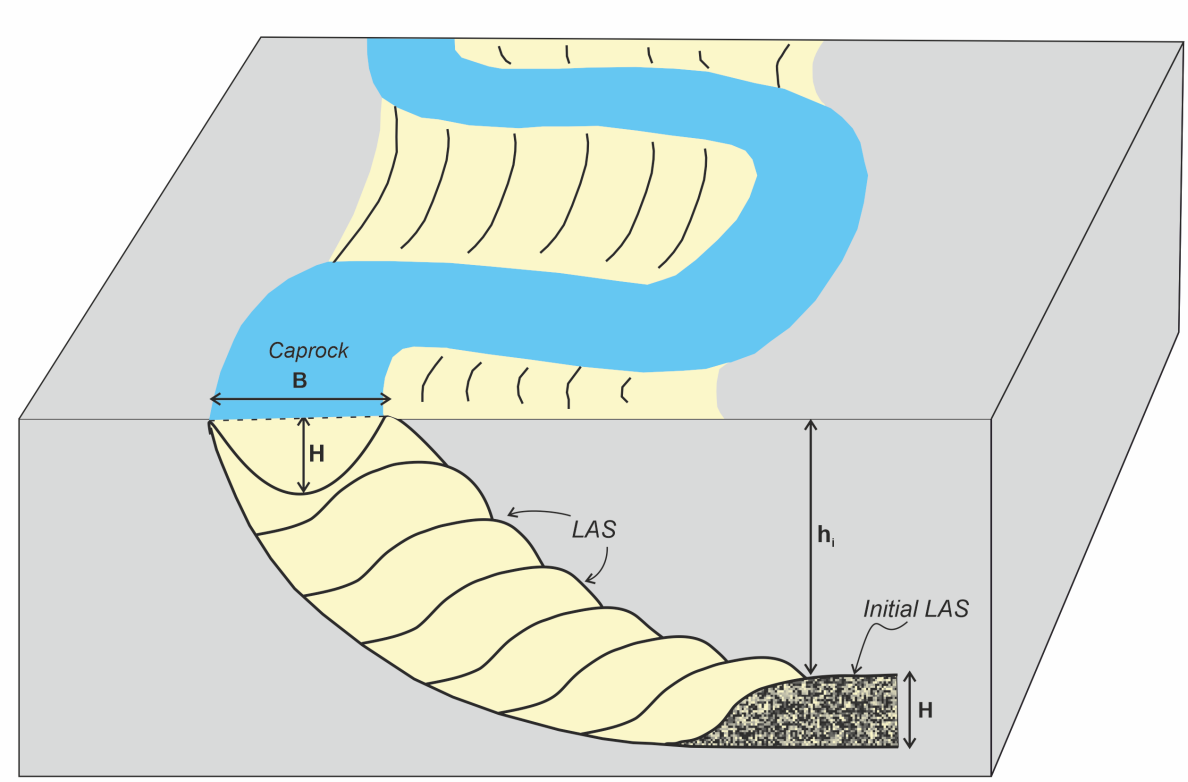

Figure S5. 3D schematic of Martian LAPs as they appear in the deposits on AD1. Individual LASs aggrade vertically from the inside bank to outside bank (right to left). The initial LAS is only visible from the top of the LAS, while its actual channel depth (shaded black) is buried. Each LAS is schematically shown to be of equal depth in the LAP. The caprock is vertically elevated (shaded blue) with the surficial point bar topography (now eroded) in beige around the caprock. Measurements for channel depth (*H*), the elevation change between the intitial LAS and caprock crest (h_i) and caprock width (*B*) are indicated. The figure has been adapted from Jobe et al. (2016).

Ahmed, J., Peakall, J., Balme, M.R., and Parsons, D.R., 2023, Rapid megaflood-triggered base-level rise on Mars: Geology, https://doi.org/10.1130/ G50277.1

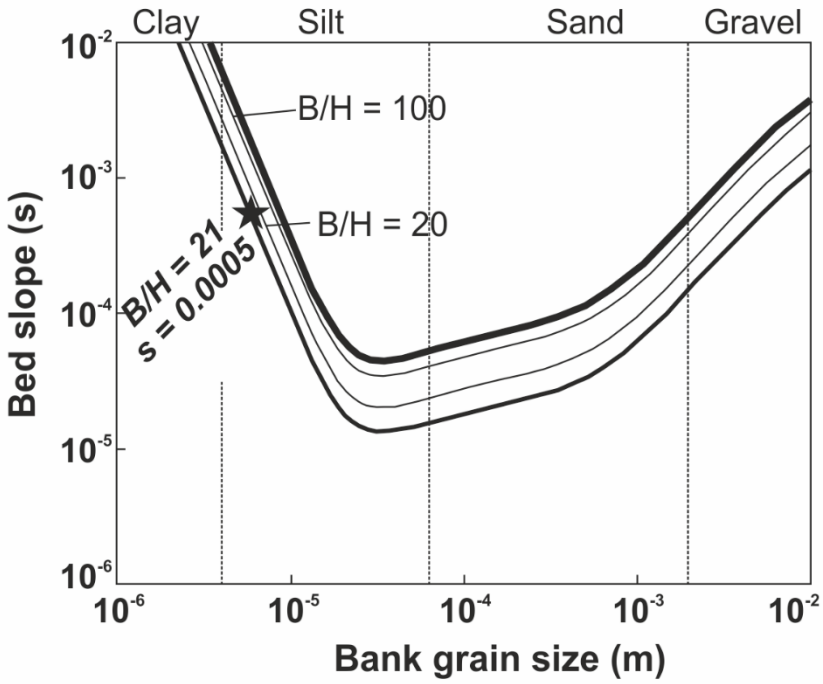

Figure S6. Predicted stability field diagram relating bank grain size to bed slope for Martian rivers assuming the properties of water at 25°C as adapted from Lapôtre et al. (2019). The width-to-depth (*B/H*) contours are shown in black, while the black star indicates the estimated position within the stability field for AD1 based on estimates of *B/H* and channel bed slope (*s*). **See Supplementary Materials and Methods** for a description of how *s* and *H* are estimated.

Figure S7. Estimated backwater lengths for AD1 from a downstream basin. Backwater lengths were estimated from measured caprock widths at the 10th (B_{10}), 50th (B_{50}), and 90th (B_{90}) percentiles and inserted into equations 2 and 3 to estimate channel depth and slope. These were divided to estimate the backwater length (B_L). Black stars represent the required increase in channel width to satisfy the observed 40 km backwater length.

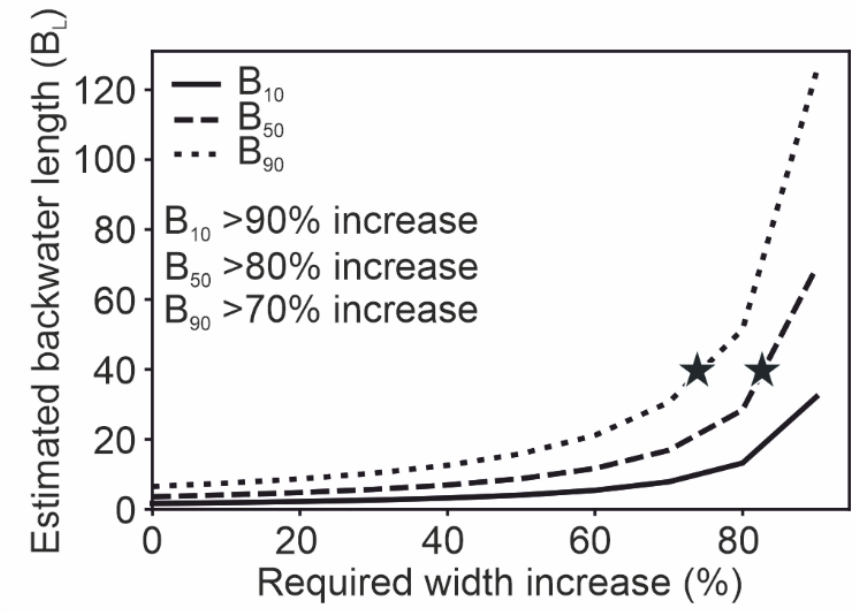

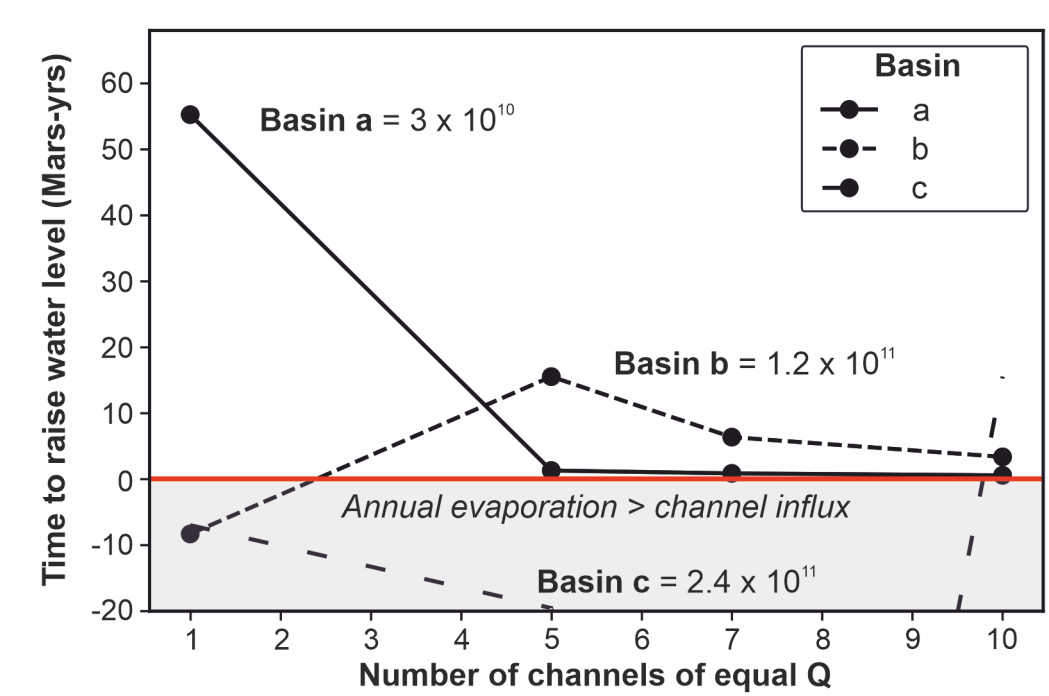

Figure S8. Estimated basin filling times for three illustrative basins (a, b, and c). Basin filling times for a, b, and c are estimated assuming constant bankfull discharge (93.4 $m^3 s^{-1}$) for the case of one, five, seven, and ten channels (black points along each line) of equal proportion. Each line illustrates the time taken for a given number of channels to raise a particular basin by 6 m as described by the legend. The horizontal red line that intersects at y=0 describes the threshold below which evaporation (assumed to be a conservative 1 m $Mars\text{-}yr^{-1}$, see rationale above) exceeds the channel influx to the basin.

Table S1. Total number of LASs identified using a manual and automated method. The manual method used peak counting from cross-sectional profiles in a Geographic Information System (GIS), while the adaptive thresholding technique utilized automated binary image segmentation to identify changes in image lighting (peaks and troughs) (Strick et al., 2018; OpenCV, 2021). Max pixels, block size, and C value all apply to the adaptive thresholding method and were used to inform the algorithm. No. of LASs indicates how many LASs were identified using each method. The paired values were compared using a Kruskal-Wallis (KW) and Student's t-test and found no significant difference ($p>0.7$) between the number of surfaces identified using each method.

		Manual method - GIS based	**Adaptive Thresholding**		
Meander	**Max pixels**	**No. of LASs**	**Block size**	**C value**	**No. of LASs**
AD1-1	255	14	15	2	17
AD1-2	255	9	15	2	12
AD1-3	255	17	15	2	19
AD1-4	255	7	9	2	9
AD1-5	255	8	15	2	8
AD1-6	255	10	9	2	10
AD1-7	255	14	9	2	13
AD1-8	255	20	15	2	20
AD1-9	255	18	15	2	20
AD1-10	255	18	15	2	13
AD1-11	255	11	9	2	13
AD1-12	255	8	9	2	8
AD1-13	255	20	15	2	17
AD1-14	255	9	9	2	12
AD1-15	255	18	9	2	16
AD1-16	255	16	15	2	16
AD1-17	255	9	9	2	10
KW test p-value = 0.74					
t-test p-value = 0.75					

Table S2 Data table showing inputs for calculation of superelevation index for bends on AD1 on Mars, and for subaerial and submarine channels on Earth. This is attached as a separate data table compiled from Jobe et al. (2020) for submarine channels, and herein for subaerial systems (sources given in **Table S3**) and including the measurements from AD1 from the present study. Note that for the column headed 'levee thickness' this is true for the subaerial and submarine channels on Earth, but that for the AD1 channel bends on Mars this refers to the thickness from the base of the lateral accretion package (LAP) to the top of the caprock – see main text for details.

Table S3. Data sources used for terrestrial levee thickness calculations.

River	No. measurements	Data Source
Colombia River, Canada	24	Filgueira-Rivera et al. (2007)
Saskatchewan River, Canada	6	Smith and Pérez-Arlucea (2008)
Columbia River/Saskatchewan River, Canada	43	Adams et al. (2004)
Muscatatuck River, Indiana	1442	Johnston et al. (2019)

Table S4. Measured and estimated AD1 channel parameters.

Variable	Value
Channel depth *(H)*	1.83 m
Average channel width *(B)*	38.81 m
Bankfull discharge *(Q)*	93.38 $m^3\ s^{-1}$
Slope *(s)*	0.00050
Friction coefficient *(C_f)*	0.002
Martian gravitational acceleration *(g_M)*	3.73 $m^2\ s^{-1}$

Table S5. Estimates of bankfull meander migration ($M_{R,M,BF}$) rate for AD1.

Variable	Width (m)	Estimated $M_{R,M,BF}$ (m yr^{-1})
10^{th} percentile channel width *(B_{10})*	21.36	132.37
Average channel width *(B_{50})*	38.80	219.90
90^{th} percentile channel width *(B_{90})*	61.65	325.91

Table S6. Estimated basin filling times for different flood volumes and discharges.

Basin	Basin volume (km^3)	Flood discharge ($m^3\ s^{-1}$)			
		1000000	100000	10000	1000
		No. days to fill basin			
a6	30	0.35	3.47	34.72	347.22
b6	120	1.39	13.89	138.89	1388.89
c6	240	2.78	27.78	277.78	2777.78

Table S7. Estimated filling times for basins a, b, and c under constant AD1 bankfull discharge conditions. Filling times were estimated for the case of 1, 5, 7, and 10 channels

feeding each basin assuming a constant bankfull discharge of 93.4 m^3 s^{-1} for each feeder channel. The total filling time (in Martian years, Mars-yrs) was estimated under assumptions of evaporation (E) and non-evaporation (NE). Negative values are indicative of basins that cannot fill at a rate greater than the annual rate of evaporation.

Basin	**Basin volume to be filled (x 10^9 m^3)**	**Time to raise water level by 6 m (Mars-yrs)**							
		1		**5**		**7**		**10**	
		E	**NE**	**E**	**NE**	**E**	**NE**	**E**	**NE**
a	3	55.2	5.41	1.3	1.1	0.9	0.7	0.6	0.5
b	12	-8.3	21.6	15.5	4.3	6.4	3.1	3.4	2.2
c	24	-6.9	43.3	-19.5	8.7	-199.8	6.2	15.6	4.3

References Cited

Adams, P.N., Slingerland, R.L., and Smith, N.D., 2004, Variations in natural levee morphology in anastomosed channel flood plain complexes: Geomorphology, v. 61, p. 127–142, doi:https://doi.org/10.1016/j.geomorph.2003.10.005.

Blum, M., Martin, J., Milliken, K., and Garvin, M., 2013, Paleovalley systems: Insights from Quaternary analogs and experiments: Earth-Science Reviews, v. 116, p. 128–169, doi:https://doi.org/10.1016/j.earscirev.2012.09.003.

Bouley, S., Baratoux, D., Matsuyama, I., Forget, F., Séjourné, A., Turbet, M., and Costard, F., 2016, Late Tharsis formation and implications for early Mars: Nature, v. 531, p. 344-347.

Bresse, J.A.C., 1860, Cours de Mecanique Appliquee, Hydraulique:

Buhler, P.B., Fassett, C.I., Head III, J.W., and Lamb, M.P., 2014, Timescales of fluvial activity and intermittency in Milna Crater, Mars: Icarus, v. 241, p. 130-147, doi.org/10.1016/j.icarus.2014.06.028.

Burr, D.M., Williams, R.M.E., Wendell, K.D., Chojnacki, M., and Emery, J.P., 2010, Inverted

fluvial features in the Aeolis/Zephyria Plana region, Mars: Formation mechanism and initial paleodischarge estimates: Journal of Geophysical Research: Planets, v. 115, doi:10.1029/2009JE003496.

Burr, D.M., Jacobsen, R.E., Lefort, A., Borden, R.M., and Peel, S.E., 2021, Geologic map of the Aeolis Dorsa Region, Mars: U.S. Geological Survey Scientific Investigations Map 3480.

Cardenas, B.T., Mohrig, D., and Goudge, T.A., 2018, Fluvial stratigraphy of valley fills at Aeolis Dorsa, Mars: Evidence for base-level fluctuations controlled by a downstream water body: GSA Bulletin, v. 130, p. 484–498, doi:10.1130/B31567.1.

Carson, M.A., and Lapointe, M.F., 1983, The Inherent Asymmetry of River Meander Planform: The Journal of Geology, v. 91, p. 41–55, doi:10.2307/30060514.

Chow, V.T., 1959, Open-channel hydraulics: 680 p.

Citron, R.I., Manga, M., and Hemingway, D.J., 2018, Timing of oceans on Mars from shoreline deformation: Nature, v. 555, p. 643-646.

DiBiase, R.A., Limaye, A.B., Scheingross, J.S., Fischer, W.W., and Lamb, M.P., 2013, Deltaic deposits at Aeolis Dorsa: Sedimentary evidence for a standing body of water on the northern plains of Mars: Journal of Geophysical Research: Planets, v. 118, p. 1285–1302, doi:10.1002/jgre.20100.

Filgueira-Rivera, M., Smith, N.D., and Slingerland, R.L., 2007, Controls on natural levée development in the Columbia River, British Columbia, Canada: Sedimentology, v. 54, p. 905–919, doi:10.1111/j.1365-3091.2007.00865.x.

Ganti, V., Chadwick, A.J., Hassenruck-Gudipati, H.J., and Lamb, M.P., 2016, Avulsion cycles and their stratigraphic signitaure on an experimental backwater-controlled delta: Journal of Geophysical Research-Earth Surface, v. 121, p. 1651-1675, doi:10.1002/2016JF003915.

Hajek, E., and Wolinsky, M.A., 2012, Simplified process modeling of river avulsions and alluvial architecture: Connecting models and field data: Sedimentary Geology, v. 257-260, p. 1-30, doi:10.1016/j.sedgeo.2011.09.005.

Hayden, A.T., and Lamb, M.P., 2020, Fluvial Sinuous Ridges of the Morrison Formation, USA: Meandering, Scarp Retreat, and Implications for Mars: Journal of Geophysical Research: Planets, v. 125, p. e2020JE006470, doi:https://doi.org/10.1029/2020JE006470.

Hayden, A.T., Lamb, M.P., Fischer, W.W., Ewing, R.C., McElroy, B.J., and Williams, R.M.E., 2019, Formation of sinuous ridges by inversion of river-channel belts in Utah, USA, with implications for Mars: Icarus, v. 332, p. 92–110, doi:https://doi.org/10.1016/j.icarus.2019.04.019.

Hughes, C.M., Cardenas, B.T., Goudge, T.A., and Mohrig, D., 2019, Deltaic deposits indicative of a paleo-coastline at Aeolis Dorsa, Mars: Icarus, v. 317, p. 442–453, doi:https://doi.org/10.1016/j.icarus.2018.08.009.

Ahmed, J., Peakall, J., Balme, M.R., and Parsons, D.R., 2023, Rapid megaflood-triggered base-level rise on Mars: Geology, https://doi.org/10.1130/ G50277.1

Ielpi, A., and Lapôtre, M.G.A., 2020, A tenfold slowdown in river meander migration driven by plant life: Nature Geoscience, v. 13, p. 82–86, doi:10.1038/s41561-019-0491-7.

Ielpi, A., Lapôtre, M.G.A., Gibling, M.R., and Boyce, C.K., 2022, The impact of vegetation on meandering rivers: Nature Reviews Earth & Environment, doi:10.1038/s43017-021-00249-6.

Jerolmack, D.J., and Mohrig, D., 2007, Conditions for branching in depositional rivers: Geology, v. 35, p. 463–466, doi.org/10.1130/G23308A.1.

Jobe, Z.R., Howes, N.C., and Auchter, N.C., 2016, Comparing submarine and fluvial channel kinematics: Implications for stratigraphic architecture: Geology, v. 44, p. 931–934, doi:10.1130/G38158.1

Jobe, Z.R., Howes, N.C., Straub, K.M., Cai, D., Deng, H., Laugier, F.J., Pettinga, L.A., and Shumaker, L.E., 2020, Comparing aggradation, superelevation, and avulsion frequency of submarine and fluvial channels: Frontiers in Earth Science, v. 8, p. 53, https://www.frontiersin.org/article/10.3389/feart.2020.00053.

Johnston, G.H., David, S.R., and Edmonds, D.A., 2019, Connecting fluvial levee deposition to flood-basin hydrology: Journal of Geophysical Research: Earth Surface, v. 124, p. 1996–2012, doi:10.1029/2019JF005014.

Kirk, R.L. et al., 2008, Ultrahigh resolution topographic mapping of Mars with MRO HiRISE stereo images: Meter-scale slopes of candidate Phoenix landing sites: Journal of Geophysical Research: Planets, v. 113, doi:10.1029/2007JE003000.

Kite, E.S., Lucas, A., and Fassett, C.I., 2013, Pacing early Mars river activity: Embedded craters in the Aeolis Dorsa region imply river activity spanned ≳(1–20)Myr: Icarus, v. 225, p. 850–855, doi:https://doi.org/10.1016/j.icarus.2013.03.029.

Konsoer, K.M., LeRoy, J., Burr, D., Parker, G., Jacobsen, R., and Turmel, D., 2018, Channel slope adjustment in reduced gravity environments and implications for Martian channels: Geology, v. 46, p. 183–186, doi:10.1130/G39666.1.

Lamb, M.P., Nittrouer, J.A., Mohrig, D., and Shaw, J., 2012, Backwater and river plume controls on scour upstream of river mouths: Implications for fluvio-deltaic morphodynamics: Journal of Geophysical Research: Earth Surface, v. 117, doi:https://doi.org/10.1029/2011JF002079.

Lapôtre, M.G.A., and Ielpi, A., 2020, The Pace of Fluvial Meanders on Mars and Implications for the Western Delta Deposits of Jezero Crater: AGU Advances, v. 1, p. e2019AV000141, doi:10.1029/2019AV000141.

Lapôtre, M.G.A., Ielpi, A., Lamb, M.P., Williams, R.M.E., and Knoll, A.H., 2019, Model for the Formation of Single-Thread Rivers in Barren Landscapes and Implications for Pre-Silurian and Martian Fluvial Deposits: Journal of Geophysical Research: Earth Surface, v. 124, p. 2757– 2777, doi:10.1029/2019JF005156.

Leeder, M.R., 1973, Fluviatile fining-upwards cycles and the magnitude of palaeochannels: Geological Magazine, v. 110, p. 265-276, doi:10.1017/S0016756800036098.

Ahmed, J., Peakall, J., Balme, M.R., and Parsons, D.R., 2023, Rapid megaflood-triggered base-level rise on Mars: Geology, https://doi.org/10.1130/ G50277.1

Lefort, A., Burr, D. M., Beyer, R. A., and Howard, A. D., 2012, Inverted fluvial features in the Aeolis-Zephyria Plana, western Medusae Fossae Formation, Mars: Evidence for post-formation modification: Journal of Geophysical Research, 117, E03007, doi: 10.1029/2011JE004008.

Li, J., Tooth, S., and Yao, G., 2019, Cascades of sub-decadal, channel-floodplain changes in low-gradient, non-vegetated reaches near a dryland river terminus: Salar de Uyuni, Bolivia: Earth Surface Processes and Landforms, v. 44, p. 490–506, doi:https://doi.org/10.1002/esp.4512.

Liu, Z., Liu, Y., Pan, L., Zhao, J., Kite, E.S., Wu, Y., and Zou, Y., 2021, Inverted channel belts and floodplain clays to the East of Tempe Terra, Mars: Implications for persistent fluvial activity on early Mars: Earth and Planetary Science Letters, v. 562, p. 116854, doi:https://doi.org/10.1016/j.epsl.2021.116854.

Matsubara, Y., Howard, A.D., Burr, D.M., Williams, R.M.E., Dietrich, W.E., and Moore, J.M., 2015, River meandering on Earth and Mars: A comparative study of Aeolis Dorsa meanders, Mars and possible terrestrial analogs of the Usuktuk River, AK, and the Quinn River, NV: Geomorphology, v. 240, p. 102–120, doi:http://dx.doi.org/10.1016/j.geomorph.2014.08.031.

Mohrig, D., Heller, P.L., Paola, C., and Lyons, W.J., 2000, Interpreting avulsion process from ancient alluvial sequences: Guadalope-Matarranya system (northern Spain) and Wasatch Formation (western Colorado): Bulletin of the Geological Society of America, v. 112, p. 1787-1803, doi:10.1130/00167606(2000)112<1758:IAPFAA>2.0.CO;2.

Morton, F.J., 1983, Operational estimates of lake evaporation: Journal of Hydrology, v. 66, p. 77-100, doi:10.1016/0022-1694(83)90178-6.

Nittrouer, J.A., Shaw, J., Lamb, M.P., and Mohrig, D., 2012, Spatial and temporal trends for water-flow velocity and bed-material sediment transport in the lower Mississippi River: GSA Bulletin, v. 124, p. 400–414, doi:10.1130/B30497.1.

OpenCV, 2021, Image Thresholding:, https://docs.opencv.org/master/d7/d4d/tutorial_py_thresholding.html (accessed November 2021).

Peakall, J., Ashworth, P.J., and Best, J.L., 2007, Meander-Bend Evolution, Alluvial Architecture, and the Role of Cohesion in Sinuous River Channels: A Flume Study: Journal of Sedimentary Research, v. 77, p. 197–212, doi:10.2110/jsr.2007.017.

Rivera-Hernández, F., and Palucis, M.C., 2019, Do deltas along the crustal dichotomy boundary of Mars in the Gale Crater region record a Northern Ocean? Geophysical Research Letters, v. 46, p. 8689–8699, doi:10.1029/2019GL083046.

Salese, F., McMahon, W.J., Balme, M.R., Ansan, V., Davis, J.M., and Kleinhans, M.G., 2020, Sustained fluvial deposition recorded in Mars' Noachian stratigraphic record: Nature Communications, v. 11, p. 2067, doi:10.1038/s41467-020-15622-0.

Santos, M.G.M., Hartley, A.J., Mountney, N.P., Peakall, J., Owen, A., Merino, E.R., and Assine, M.L., 2019, Meandering rivers in modern desert basins: Implications for

channel planform controls and prevegetation rivers: Sedimentary Geology, v. 385, p. 1–14, doi:/10.1016/j.sedgeo.2019.03.011.

Shiers, M.N., Mountney, N.P., Hodgson, D.M., and Colombera, L., 2019, Controls on the depositional architecture of fluvial point-bar elements in a coastal-plain succession. In: Ielpi, A., Ghinassi, M., Rainbird, R.H., and Ventra, D. (Eds.), Fluvial meanders and their sedimentary products in the rock record. Hoboken, NJ: International Association of Sedimentologists, 48, p. 15-46. doi:10.1002/9781119424437.

Smith, N.D., and Pérez-Arlucea, M., 2008, Natural levee deposition during the 2005 flood of the Saskatchewan River: Geomorphology, v. 101, p. 583–594, doi:https://doi.org/10.1016/j.geomorph.2008.02.009.

Strick, R.J.P., Ashworth, P.J., Awcock, G., and Lewin, J., 2018, Morphology and spacing of river meander scrolls: Geomorphology, v. 310, p. 57–68, doi:https://doi.org/10.1016/j.geomorph.2018.03.005.

Swartz, J.M., Goudge, T.A., and Mohrig, D.C., 2020, Quantifying coastal fluvial morphodynamics over the last 100 years on the lower Rio Grande, USA and Mexico: Journal of Geophysical Research: Earth Surface, v. 125, e2019JF005443.

Willis, B.J., and Tang, H., 2010, Three-dimensional connectivity of point bar deposits. Journal of Sedimentary Research, v. 80, p. 440-454.

Wordsworth, R., Kalugina, Y., Lokshtanov, S., Vigasin, A., Ehlmann, B., Head, J., Sanders, C., and Wang, H., 2017, Transient reducing greenhouse warming on early Mars: Geophysical Research Letters, v. 44, p. 665–671, doi:https://doi.org/10.1002/2016GL071766.

Wright, S., and Parker, G., 2004, Flow Resistance and Suspended Load in Sand-Bed Rivers: Simplified Stratification Model: Journal of Hydraulic Engineering, v. 130, p. 796–805, doi:10.1061/(ASCE)0733-9429(2004)130:8(796).

Yan, N., Colombera, L., and Mountney, N.P., 2021, Controls on fluvial meander-belt thickness and sand distribution: Insights from forward stratigraphic modelling: Sedimentology, v. 68, p. 1831-1860.